Towards a Comprehensive View of Accretion, Inner Disks, and Extinction in Classical T Tauri Stars: An ODYSSEUS Study of the Orion OB1b Association

Caeley V. Pittman, Catherine C. Espaillat, Connor E. Robinson, Thanawuth Thanathibodee, Nuria Calvet, John Wendeborn, Jesus Hernández, Carlo F. Manara, Fred Walter, Péter Ábrahám, et al.

The Astronomical Journal, 164:201 (16pp), 2022 November https://doi.org/10.3847/1538-3881/ac898d

Towards a Comprehensive View of Accretion, Inner Disks, and Extinction in Classical T Tauri Stars: An ODYSSEUS Study of the Orion OB1b Association

Caeley V. Pittman[1], Catherine C. Espaillat[1], Connor E. Robinson[2], Thanawuth Thanathibodee[1], Nuria Calvet[3], John Wendeborn[1], Jesus Hernández[4], Carlo F. Manara[5], Fred Walter[6], Péter Ábrahám[7,8,9], Juan M. Alcalá[10], Sílvia H. P. Alencar[11], Nicole Arulanantham[12], Sylvie Cabrit[13], Jochen Eislöffel[14], Eleonora Fiorellino[7,9,10], Kevin France[15], Manuele Gangi[16], Konstantin Grankin[17], Gregory J. Herczeg[18,19], Ágnes Kóspál[7,8,9,20], Ignacio Mendigutía[21], Javier Serna[4], and Laura Venuti[22]

[1] Institute for Astrophysical Research, Department of Astronomy, Boston University, 725 Commonwealth Avenue, Boston, MA 02215, USA; cpittman@bu.edu
[2] Department of Physics & Astronomy, Amherst College, Amherst, MA 01002, USA
[3] Department of Astronomy, University of Michigan, 311 West Hall, 1085 S. University Avenue, Ann Arbor, MI 48109, USA
[4] Instituto de Astronomía, Universidad Autónoma de México Ensenada, B.C, MÉxico
[5] European Southern Observatory, Karl-Schwarzschild-Strasse 2, 85748 Garching, Germany
[6] Department of Physics and Astronomy, Stony Brook University, Stony Brook, NY 11794-3800, USA
[7] Konkoly Observatory, Research Centre for Astronomy and Earth Sciences, Eötvös Loránd Research Network, Konkoly-Thege Miklós út 15-17, 1121 Budapest, Hungary
[8] ELTE Eötvös Loránd University, Institute of Physics, Pázmány Péter Sétány 1/A, 1117 Budapest, Hungary
[9] CSFK, MTA Centre of Excellence, Konkoly-Thege Miklós út 15-17, 1121 Budapest, Hungary
[10] Osservatorio Astronomico di Capodimonte, via Moiariello 16, 80131 Napoli, Italy
[11] Departamento de Física, Universidade Federal de Minas Gerais, Av. Antonio Carlos 6627, 30270-901 Belo Horizonte, MG, Brazil
[12] Space Telescope Science Institute, 3700 San Martin Drive, Baltimore, MD 21218, USA
[13] Observatoire de Paris, PSL University, Sorbonne University, CNRS, LERMA, 61 Av. de l'Observatoire, 75014 Paris, France
[14] Thüringer Landessternwarte, Sternwarte 5, D-07778 Tautenburg, Germany
[15] Laboratory for Atmospheric and Space Physics, University of Colorado Boulder, Boulder, CO 80303, USA
[16] Osservatorio Astronomico di Roma, via di Frascati 33, 00078 Monte Porzio Catone, Italy
[17] Crimean Astrophysical Observatory, Department of Stellar Physics, Nauchny, 298409, Crimea†
[18] Kavli Institute for Astronomy and Astrophysics, Peking University, Yiheyuan 5, Haidian Qu, 100871 Beijing, People's Republic of China
[19] Department of Astronomy, Peking University, Yiheyuan 5, Haidian Qu, 100871 Beijing, People's Republic of China
[20] Max Planck Institute for Astronomy, Königstuhl 17, 69117 Heidelberg, Germany
[21] Centro de Astrobiología (CSIC-INTA), ESA-ESAC Campus, 28692, Villanueva de la Cañada, Madrid, Spain
[22] SETI Institute, 339 Bernardo Ave., Suite 200, Mountain View, CA 94043, USA
Received 2022 June 15; revised 2022 August 2; accepted 2022 August 7; published 2022 October 18

Abstract

The coevolution of T Tauri stars and their surrounding protoplanetary disks dictates the timescales of planet formation. In this paper, we present magnetospheric accretion and inner disk wall model fits to near-UV (NUV) to near-IR (NIR) spectra of nine classical T Tauri stars in Orion OB1b as part of the Outflows and Disks around Young Stars: Synergies for the Exploration of ULLYSES Spectra (ODYSSEUS) survey. Using NUV–optical spectra from the Hubble UV Legacy Library of Young Stars as Essential Standards (ULLYSES) Director's Discretionary Program and optical–NIR spectra from the PENELLOPE VLT Large Programme, we find that the accretion rates of these targets are relatively high for the region's intermediate age of 5.0 Myr; rates are in the range of $(0.5–17.2) \times 10^{-8}\ M_{\odot}\,\mathrm{yr}^{-1}$, with a median value of $1.2 \times 10^{-8}\ M_{\odot}\,\mathrm{yr}^{-1}$. The NIR excesses can be fit with 1200–1800 K inner disk walls located at 0.05–0.10 au from the host stars. We discuss the significance of the choice in extinction law, as the measured accretion rate depends strongly on the adopted extinction value. This analysis will be extended to the complete sample of T Tauri stars being observed through ULLYSES to characterize accretion and inner disks in star-forming regions of different ages and stellar populations.

Unified Astronomy Thesaurus concepts: Pre-main sequence stars (1290); Stellar accretion (1578); Stellar accretion disks (1579); Protoplanetary disks (1300); Reddening law (1377); Interstellar extinction (841); Hubble Space Telescope (761); Very Large Telescope (1767)

Supporting material: data behind figure, machine-readable tables

1. Introduction

The coevolution of T Tauri stars (TTSs) and their surrounding protoplanetary disks is one of the most important subjects in the field of planet formation (Manara et al. 2022). Accretion of disk material onto the star can be traced by continuum excesses in the near-UV (NUV) to optical region of the spectrum (Valenti et al. 1993; Gullbring et al. 2000; Herczeg & Hillenbrand 2008). Emission from the frontally illuminated inner wall of the disk can be traced by continuum excesses in the near-IR (NIR) to mid-IR (MIR) region (Natta et al. 2001; Tuthill et al. 2001;

† While the AAS journals adhere to and respect UN resolutions regarding the designations of territories (available at http://www.un.org/press/en), it is our policy to use the affiliations provided by our authors on published articles.

D'Alessio et al. 2005). A model that can self-consistently reproduce the spectra of actively accreting TTSs from the UV to the IR is a vital tool for understanding the coevolution of the star and inner disk. To reproduce the NUV–NIR spectra of classical TTSs (CTTSs), one can combine accretion shock and inner disk wall models to create a consistent description of the physical mechanisms producing the observed spectra, as has been demonstrated in GM Aurigae by Ingleby et al. (2015).

The magnetospheric accretion model (Koenigl 1991; Shu et al. 1994; Hartmann et al. 1994; Calvet & Gullbring 1998; Muzerolle et al. 1998, 2001) has been widely used in explaining observations of UV excesses and emission lines in CTTSs (for a review, see Hartmann et al. 2016). Bouvier et al. (2020) and the Gravity Collaboration (2020) confirmed that hydrogen Brγ emission associated with the magnetospheric accretion paradigm originates well within TTS corotation radii, reinforcing the hypothesis that the emission comes from accretion columns rather than a wind farther away from the star. When modeling this emission, it is important to fit the optical spectra in addition to the NUV, as accretion estimates that fit excesses only at blue wavelengths underestimate the accretion rates by a factor of $\sim$2 (Fischer et al. 2011). To account for both NUV and optical continuum excesses in CTTSs, Ingleby et al. (2013) found that a multicolumn accretion shock model should be used (based on the shock model of Calvet & Gullbring 1998).

D'Alessio et al. (2005) found that the spectrum of a heated inner wall of a dusty disk located at the dust sublimation radius dominates the emission at NIR−MIR wavelengths. The structure and intensity of emission from the inner wall of protoplanetary disks are determined primarily by the wall's geometry and the mineralogy of the dust (e.g., Muzerolle et al. 2003; McClure et al. 2013). Gas accretion onto the star is likely driven by turbulence in this inner disk, which also necessarily causes diffusion of dust particles that are coupled to the gas; the strength of this diffusion dictates the shape of the inner wall, independent of dust composition, with the wall geometry ranging from short and curved to tall and vertical (Schobert & Peeters 2021). The primary implication of this is that observed emission from a curved wall does not depend heavily on disk inclination i, whereas emission from a vertical wall depends strongly on i. McClure et al. (2013) best fit the 2–10 μm continuum excesses of four TTSs by approximating a curved wall using two vertical walls at different radii, each with a different height, dust size distribution, and composition.

The Hubble UV Legacy Library of Young Stars as Essential Standards (ULLYSES) DDT program (Roman-Duval et al. 2020), combined with the PENELLOPE Very Large Telescope (VLT) Large Program (Manara et al. 2021a), provides an ideal sample for exploring the variation in CTTS system properties across ranges of spectral types, ages, and masses. The Outflows and Disks around Young Stars: Synergies for the Exploration of ULLYSES Spectra (ODYSSEUS) collaboration (Espaillat et al. 2022) is maximizing the scientific impact of these data by studying accretion, outflows, and disk chemistry in the largest sample of TTSs observed with the Hubble Space Telescope (HST) to date. This paper focuses on modeling the accretion and inner disks of the first sample of TTSs observed by ULLYSES.

ULYSSES began observations with Orion OB1, located about 400 pc away (Briceño et al. 2019). Here we study nine CTTSs in the Orion OB1b star-forming region, which has a mean age of 5.0 Myr and a disk fraction of 12% (Briceño et al. 2019). This is intermediate between Cloud B (2.5 Myr, 31% CTTS) and OB1a (10.8 Myr, 6% CTTS), indicating an intermediate level of disk evolution in the region.

In this work, we model the same Orion OB1b sample of CTTSs as Manara et al. (2021a) to demonstrate the significance of using NUV spectra to determine the accretion and extinction properties of these targets. For the first time, we model both accretion and inner disks in a sample of CTTSs using contemporaneous spectra from 2000 to 24000 Å. Once this analysis is extended to the full ULLYSES sample of $\sim$60 CTTSs in nine star-forming regions, we can constrain the relationships between stellar parameters and accretion and inner disk properties to an extent that has not been done before.

This paper is organized as follows. In Section 2, we discuss the sample of TTSs, multiplicity in the sample, stellar parameters, and observations. In Section 3, we describe the accretion shock and disk models used to fit the NUV–NIR continua of the CTTSs. Section 4 presents the modeling results. In Section 5, we compare our results to those of previous studies and discuss the significance of the choice in extinction law and the wavelength range of data available. Finally, in Section 6 we present a summary of our findings and future work that will be possible through ODYSSEUS.

2. Sample and Observations

The ULLYSES program (Roman-Duval et al. 2020) began observations with a sample of eight CTTSs in the Orion OB1b subassociation (Briceño et al. 2001, 2005, 2019) and two weak-lined TTSs (WTTSs; nonaccreting sources) in the 25 Ori cluster, which are used as template photospheres in this analysis (see Figure 3 in Appendix A for a justification of their classification as WTTSs). Each target was observed with both HST and the VLT contemporaneously. One of these targets, CVSO 165, was discovered to be a binary system composed of two CTTSs, so 11 TTSs were observed in total, spanning spectral types M3.5–K6 and masses 0.3–0.9 $M_{\odot}$.

2.1. Objects and Stellar Parameters

CVSO 17, CVSO 36, and CVSO 109 are known to be physical binaries (Tokovinin et al. 2020), and CVSO 104 and CVSO 165 have visual companions with which they are not kinematically associated (Manara et al. 2021a). The primary component of CVSO 104 was found to be a spectroscopic binary (Kounkel et al. 2019; Manara et al. 2021a; Frasca et al. 2021), but these components are not resolved in the HST observations. Proffitt et al. (2021) found that the primary component of CVSO 165 is also itself a binary. The ULLYSES HST observations of this object are able to resolve the two components, which both show signatures of active accretion and are thus both modeled in this analysis.

Stellar parameters for all CTTS targets and WTTS photospheric templates used in this work are listed in Table 2. For targets not affected by unresolved binarity in their X-Shooter observations, values for spectral type (SpT), mass ($M_{\star}$), distance (d), and veiling (r) are adopted from Manara et al. (2021a), and their values for stellar radius ($R_{\star}$) and V-band extinction (A_V) are included for comparison with the values we derive. Effective temperatures for all targets except the CVSO 165 binary system come from the temperature–spectral type relation given for 5–30 Myr stars in Pecaut & Mamajek (2013). Manara et al. (2021a) derive distances from Gaia Early

Data Release 3 parallaxes that have reliable astrometric solutions (typically RUWE < 1.4). For those without reliable solutions, the mean distance to the association is used and an uncertainty of 10% assumed.

2.1.1. CVSO 165 Binary

We obtain the effective temperature ($T_{\rm eff}$) and the visual extinction (A_V) for each component of the CVSO 165 system by comparing the HST spectra against the PHOENIX synthetic spectral library (Husser et al. 2013). We use values of surface gravity adequate for stars (e.g., $3.0 < \log(g) < 4.5$) and interpolate the spectral library to obtain theoretical grids with intervals of 50 K in $T_{\rm eff}$. For each theoretical spectrum, we apply values of A_V from 0 to 5 in steps of 0.01 using the standard interstellar reddening law ($R_V = 3.1$) from Cardelli et al. (1989). Minimizing χ^2, we obtain the $T_{\rm eff}$ and the A_V from the best match between the observed HST spectra and the reddened synthetic spectra. To avoid contamination from accretion flux, we use the spectral range from 6000 to 9000 Å. We also avoid the region around Hα, fitting a Gaussian function to the line profile and ignoring the spectral range between -5σ and $+5\sigma$ from the center of the line. Finally, the uncertainties in the estimated values are obtained using the Monte Carlo (MC) method of error propagation (Anderson 1976), varying the HST spectra fluxes randomly 500 times within their reported uncertainties. The values reported in Table 2 are the median and standard deviation of the 500 MC results.

We derive V magnitudes for each component of CVSO 165 by multiplying the HST spectrum by the Johnson V-filter transmission curve. We obtained $V = 13.875 \pm 0.002$ for CVSO 165A and $V = 15.775 \pm 0.004$ for CVSO 165B. The RUWE astrometric parameter is highly sensitive to unresolved binary systems; the high RUWE value of 14.3 for CVSO 165 indicates a poor astrometric solution (Lindegren 2020). Therefore, we assume a distance of 400 ± 40 pc (Briceño et al. 2019) to estimate the stellar luminosity for CVSO 165A and CVSO 165B using the visual magnitude corrected by extinction. Finally, comparing the location on the H-R diagram with the MIST evolutionary model (Dotter 2016), we obtained the stellar masses reported in Table 2 for each component. The uncertainties in the masses were obtained using the MC method of error propagation and the uncertainties estimated for the luminosity and $T_{\rm eff}$.

2.1.2. Veiling

Veiling measurements are necessary to set the flux of the WTTS template photosphere relative to the CTTS spectrum, with the relationship given by $F_{{\rm phot},\lambda} = F_{{\rm CTTS},\lambda}/(1 + r_\lambda)$. In our analysis, we scale the WTTS template spectrum to the data using the observed veiling at one wavelength, λ_0. First, the WTTS spectrum is scaled to the observed CTTS spectrum at λ_0 with a $\frac{F_{\rm obs}(\lambda_0)}{F_{\rm phot}(\lambda_0)}$ term. Then, it is scaled to the observed veiling with a $\frac{1}{1+r_{\lambda_0}}$ term such that the contribution of the photosphere to the data's continuum flux at λ_0 is equivalent to the contribution implied by the veiling measurement. Only the absolute flux of the WTTS template spectrum is changed, not the shape of the WTTS spectrum. This scaling process allows us to use the observed veiling to determine the amount of continuum excess emission for which we need to account with the accretion shock and inner disk wall models.

Table 1
Observation Log

Object	Telescope/Instrument	Date (MJD)
CVSO 58	HST/STIS[a]	59184.97
	VLT/X-Shooter[b]	59185.25
	VLT/UVES[b,c]	59185.09
CVSO 90	HST/STIS[a]	59199.60
	VLT/X-Shooter[b,c]	59198.06
CVSO 104	HST/STIS[a]	59180.21
	VLT/X-Shooter[b]	59180.13
	VLT/UVES[b,c]	59179.12
CVSO 107	HST/STIS[a]	59188.02
	VLT/X-Shooter[b]	59187.08
	VLT/UVES[b,c]	59188.14
CVSO 109	HST/STIS[a]	59181.20
	VLT/X-Shooter[b]	59181.15
	VLT/UVES[b,c]	59181.17
CVSO 146	HST/STIS[a]	59192.85
	VLT/X-Shooter[b]	59192.08
	VLT/ESPRESSO[b,c]	59193.09
CVSO 165	HST/STIS[a]	59197.82
	VLT/X-Shooter[b]	59197.08
	VLT/ESPRESSO[b,c]	59198.10
CVSO 176	HST/STIS[a]	59182.86
	VLT/X-Shooter[b]	59185.17
	VLT/UVES[b,c]	59183.15

Notes.
[a] Observed through the ULLYSES HST DDT Program (Roman-Duval et al. 2020).
[b] Observed through the PENELLOPE VLT Large Programme (Manara et al. 2021a).
[c] Used for veiling measurement.

Three epochs of veiling measurements at $\lambda_0 = 5500$ Å (r_{5500}) are available for seven out of nine of the CTTSs from VLT/UVES and VLT/ESPRESSO (Manara et al. 2021a), and we use the value from the epoch closest in time to the HST/STIS observations for these targets. CVSO 90 has VLT/X-Shooter veiling available at $\lambda_0 = 7100$ Å, so this is used in place of r_{5500} for this target. The veiling measured from the unresolved CVSO 165 spectrum is split between the two components according to the ratio of their U-band fluxes. CVSO 104 has not yet been formally modeled at the wavelengths relevant to accretion; however, its r_{5500} has been estimated from modeling the UVES spectrum when the objects are nearly in conjunction (A. Frasca, private communication). The observations used to measure the veiling for each target are shown in Table 1, and the veiling values are included in Table 2.

2.2. Hubble Space Telescope/STIS Observations

HST Space Telescope Imaging Spectrograph (STIS) and Cosmic Origins Spectrograph (COS) observations of these targets were taken as part of the ULLYSES DDT program through proposals GO16113, GO16114, and GO16115 (Roman-Duval et al. 2020; PI: Julia Roman-Duval). This paper utilizes observations of each target with the following gratings:

Table 2
Adopted Stellar Properties of Orion OB1 Targets

Object	SpT	Temperature (K)	Luminosity ($L_\odot$)	Radius ($R_\odot$)	Mass ($M_\odot$)	Distance (pc)	A_V (mag)	r	Template
				Single CTTSs					
CVSO 58	K7	3970	0.32	1.19	0.81	349.00 ± 2.8	0.8	0.81 ± 0.04	HBC 427+*TWA 6*
CVSO 90	M0.5	3700	0.13	0.88	0.62	$338.70^{+3.8}_{-3.7}$	0.1	1.8 ± 0.4[f]	TWA 7+*TWA 14*
CVSO 107	M0.5	3700	0.32	1.38	0.53	330.40 ± 2.5	0.3	0.98 ± 0.11	TWA 7+*TWA 14*
CVSO 146	K6	4020	0.80	1.84	0.86	332.00 ± 1.7	0.6	0.44 ± 0.10	HBC 427+*RXJ1543.1-3920*
CVSO 176	M3.5	3260	0.34	1.83	0.25	$302.40^{+2.9}_{-2.8}$	1.0	0.34 ± 0.16	CVSO 17/36+*TWA 15A*
				Binary CTTSs					
CVSO 104[e]	M2	3490	0.37	1.66	0.37	$360.70^{+3.9}_{-3.8}$	0.2	0.8[h]	CVSO 17/36+*TWA 2A*
CVSO 109A[a]	M0 ± 0.5	3767.6 ± 81.2	$0.59^{+0.17}_{-0.13}$	1.81 ± 0.25	$0.50^{+0.07}_{-0.05}$	400 ± 40	$0.06^{+0.24}_{-0.24}$	0.90 ± 0.08	TWA 7+*TWA 14*
CVSO 165A	$K5.5 \pm 1.0$	4221 ± 28	$0.90^{+0.19}_{-0.15}$	1.78 ± 1.07	0.84 ± 0.05	400 ± 40	0.32 ± 0.05	0.21 ± 0.03[g]	RECX 1+*RXJ1543.1-3920*
CVSO 165B	$M1 \pm 1.5$	3849 ± 7	$0.47^{+0.10}_{-0.08}$	1.55 ± 0.93	0.58 ± 0.23	400 ± 40	1.35 ± 0.12	0.15 ± 0.02[g]	TWA 7+*TWA 14*
				WTTSs					
RECX 1[b]	K5	4140	1.0	1.8	0.9	97	0.0	…	…
RX J1543.1–3920[c]	K6	4020	0.40	1.19	…	150	0.1 ± 0.1	…	…
HBC 427[b]	K7	3970	0.8	1.9	0.8	140	0.0	…	…
TWA 6[d]	K7	3970	0.11	0.67	0.66	51	…	…	…
TWA 14[d]	M0.5	3700	0.15	0.90	0.73	96	…	…	…
TWA 7[b]	M1	3630	0.5	1.8	0.5	50	0.0	…	…
TWA 2A[d]	M2	3490	0.33	1.51	0.55	47	…	…	…
CVSO 17[e]	M2	3490	0.30	1.50	0.37	$414.2^{+9.3}_{-8.9}$	0.0	…	…
CVSO 36[e]	M2	3490	0.22	1.28	0.39	335.5 ± 3.0	0.1	…	…
TWA 15A[d]	M3.5	3260	0.11	1.00	0.30	111	…	…	…

Notes. The following stellar parameters for the CTTSs come from Manara et al. (2021a) unless otherwise noted: spectral type, luminosity, mass, distance (derived from GAIA Early Data Release 3 parallaxes when reliable solutions were available; see Gaia Collaboration et al. 2021), A_V, and r. All veilings are at 5500 Å unless otherwise noted. The adopted temperature comes from the temperature–spectral type relation for 5–30 Myr stars in Pecaut & Mamajek (2013, Table 6), with an average used for intermediate spectral types. The radius is calculated from the luminosity and temperature using the Stefan–Boltzmann relation. Italicized WTTSs come from X-Shooter; otherwise, they come from HST/STIS. The average of CVSO 17 and CVSO 36, weighted by their uncertainties, is used because the individual spectra have low signal-to-noise ratio in the NUV.

[a] Espaillat et al. (2022).
[b] Ingleby et al. (2013).
[c] Manara et al. (2017).
[d] Manara et al. (2013).
[e] Unresolved spectroscopic binary system.
[f] Veiling at 7100 Å from X-Shooter.
[g] Veiling for the primary and secondary components of CVSO 165 attained by scaling the ESPRESSO veiling of 0.36 ± 0.05 for CVSO 165 to the ratio of the components' U-band fluxes.
[h] Veiling at 5500 Å estimated from modeling the UVES spectrum when the binary components are nearly in conjunction (A. Frasca, private communication).

STIS/G230L (spectral resolution 500–1010, plate scale 0.″025 pixel^{-1}, and NUV-MAMA pixel size of 25 μm), STIS/G430L (spectral resolution 530–1040, plate scale 0.″051 pixel^{-1}, and CCD pixel size of 21 μm), and STIS/G750L (spectral resolution 530–1040, plate scale 0.″051 pixel^{-1}, and CCD pixel size of 21 μm), all using the 52X2 slit. These spectra span a total wavelength range of 1710–10000 Å after they are combined and trimmed. See Table 1 for the times of observations. Values of λF_λ that are less than 1×10^{-15} erg s^{-1} cm^{-2} are removed. The spectra analyzed here come from ULLYSES Data Release 4, which separates spectra for the resolvable binary systems (CVSO 36, CVSO 104, CVSO 109, and CVSO 165) into their constituent components. The data between 1710 and 3300 Å are dereddened with our derived A_V using the Whittet et al. (2004) extinction law based on HD 29647 in Taurus (normalized to the Cardelli et al. 1989 standard interstellar medium (ISM) law), as the Whittet et al. (2004) law removes a potential overcorrection of the 2175 Å bump that is present in standard ISM extinction laws. From 3300 Å onward, the data are dereddened using the Cardelli et al. (1989) law to align with the analysis of Manara et al. (2021a). Both laws assume an interstellar reddening of $R_V = 3.1$.

2.3. Very Large Telescope/X-Shooter Observations

Contemporaneous VLT/X-Shooter observations were taken through the ESO PENELLOPE Large Programme (Manara

et al. 2021b, PI: Carlo Manara; see their Figures F.1 and F.2 for the X-Shooter data overplotted with the HST data). See Table 1 for the times of observations. Though observations were taken in the UVB, VIS, and NIR arms, we use only the NIR spectra (spectral resolution ∼11,600, plate scale 0.″248 pixel^{-1}, using the 0.″4 slit) for modeling the inner disk wall because HST data are available out to 1 μm. As described in Manara et al. (2021a), these flux-calibrated data are dereddened using the Cardelli et al. (1989) extinction law and corrected for telluric absorption using *molecfit* v3.0.3 (Smette et al. 2015; Kausch et al. 2015). Again, points with $\lambda F_\lambda < 1 \times 10^{-15}$ erg s^{-1} cm^{-2} are removed.

The X-Shooter data for the binary targets CVSO 109 and CVSO 165 are unresolved, so it is necessary to split the total flux between the two components to achieve a better representation of the resolved NIR spectra. As described in Espaillat et al. (2022), the X-Shooter spectrum of CVSO 109A is scaled by the *J*-band fluxes of the two components and their difference found by Tokovinin et al. (2020). The *J*-band flux difference is not available for CVSO 165A and CVSO 165B, so these spectra are simply scaled down to align with the HST continua. This is just an approximation given that the two components have different spectral types. However, our inferred NIR flux ratio of the primary to the secondary of 2.4 is reasonably consistent with our measured *V*- and *R*-band flux ratios of 2.6 and 2.7, respectively.

The HST and X-Shooter observations of CVSO 176 were separated by about 65 hr, and this seems to have produced a significant discontinuity between the data. This can likely be attributed to variability, as variations on the order of hours to days are expected from magnetosphere–disk interactions (Venuti et al. 2017; Sergison et al. 2020; Fischer et al. 2022). Both the flux and slope of the HST and X-Shooter continua do not agree. However, if the X-Shooter spectrum is scaled up by a factor of 1.75 (corresponding to a change of 0.6 mag), it aligns with the HST spectrum. This agrees with contemporaneous photometry from AAVSOnet that shows a decrease in Sloan *i*-band flux of 0.6 mag between MJD 9182.67 and 9189.84.[23] This likely indicates a change in the emission from the inner disk wall. Both the scaled and unscaled X-Shooter data are shown in the model fits to CVSO 109A, CVSO 165A, CVSO 165B, and CVSO 176 presented in Figure 1.

2.4. Transiting Exoplanet Survey Satellite Observations

The Transiting Exoplanet Survey Satellite (TESS; Ricker et al. 2014), has observed these targets on two occasions, in Sector 6 (2018 December 11 through 2019 January 07) and in Sector 32 (2020 November 19 through December 17). The latter coincided with the observations reported here, and these data were used to estimate the stellar rotation periods of our targets (expected of order 4–9 days; Percy et al. 2010). We note that the 27-day viewing window of TESS samples only a few of the expected periods, so this analysis only reveals gross trends in very complex light curves.

We download the full-frame image data from the MAST archives using the TESScut software (Brasseur et al. 2019). TESS images, while photometrically stable and of continuous cadence, suffer from coarse spatial resolution (21″ pixels). TESS is a single-channel photometer with a 600–1000 nm bandpass. The temporal resolution was 10 minutes in Sector 32 and 30 minutes in Sector 6.

We extract the data using aperture photometry with a 1.5-pixel radius. The background is extracted from an annulus between 5 and 10 pixels from the source. Because there are often other sources in the background annulus, we iterate on the background pixels, removing those more than 3σ from the median level until we converge on the median background level. We assume that the background is spatially flat in this region.

2.5. Weak-lined TTS Photospheric Templates

The template photospheres constructed for each of the CTTS targets are composed of two WTTS spectra stitched together: the wavelength range between 2000 and ∼6000 Å comes from the HST/STIS spectrum closest in spectral type to the CTTSs, and the remaining data out to 24000 Å come from the VLT/X-Shooter spectrum that provided the best photospheric fit in Manara et al. (2021a) (except for CVSO 165B, which has a spectral type different from that assigned to the unresolved CVSO 165 system). All targets have HST WTTSs within ±1 spectral subtype except for CVSO 176, which is fit with a WTTS 1.5 subtypes earlier. Each pair of WTTSs stitched together as photospheric templates for each CTTS target is listed in the "Template" column of Table 2. Note that there are four X-Shooter WTTSs for which extinction estimates are unavailable. A_V for these targets is assumed to be zero because they were chosen from regions of low extinction (Manara et al. 2013). This should not have a significant effect on the fitted A_V and $\dot{M}$ values because extinction is most important at wavelengths shorter than these X-Shooter WTTS spectra cover.

3. Accretion and Disk Models

The accretion and disk wall models used in this work are computed and fit in order to be consistent with one another. First, the accretion shock model is calculated for the specific stellar parameters of each target and fit to the data. Then, the output stellar radius, accretion rate, and shock temperature are used as inputs to the disk wall model, which is then calculated for the given stellar parameters and fit to the data. In Sections 3.1–3.2, we describe our implementation of the Calvet & Gullbring (1998) accretion shock model and the D'Alessio irradiated accretion disk (DIAD) radiative transfer model (D'Alessio et al. 1998, 1999, 2001, 2004, 2005, 2006).

3.1. Multicolumn Accretion Shock Model

We model the NUV and optical HST continua using the Calvet & Gullbring (1998) accretion shock model, updated to include three accretion columns of varying energy fluxes. These approximate a flow with a density gradient, as was recently found in GM Aurigae (Espaillat et al. 2021). Following Calvet & Gullbring (1998), we assume a magnetospheric truncation radius (R_i) of 5 $R_\star$ for all objects but CVSO 109A.[24] R_i, $R_\star$, and $M_\star$ determine the infall velocity of the accreted material, which is assumed to be the freefall velocity. The updated model is solved for individual parameter combinations rather than interpolating over a presolved grid of solutions. We add

[23] http://www.astro.sunysb.edu/fwalter/SMARTS/Odysseus/cvso176.phot.html

[24] Modeling of Hα and Hβ lines of CVSO 109A showed a smaller R_i of 2.3 $R_\star$ (see Espaillat et al. 2022), but this analysis is still in preparation for the other objects (Thanathibodee et al., in preparation). We note that changing R_i to 2.3 $R_\star$ from 5 $R_\star$ increases the calculated accretion rate by a factor of 1.4.

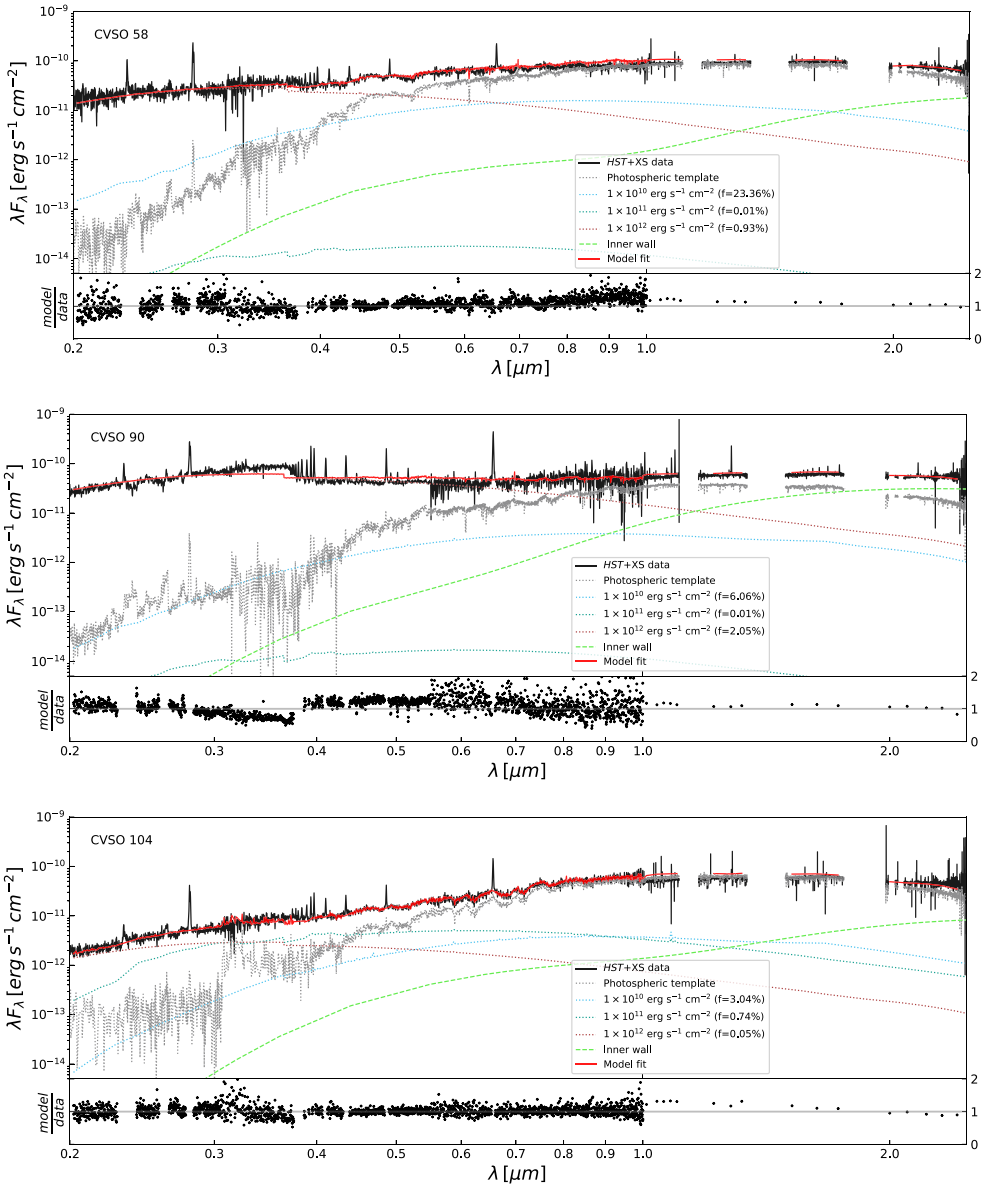

Figure 1. Fitting the NUV–NIR continua of Orion OB1b targets. We show the HST (0.2–1 μm) and X-Shooter (1–2.4 μm) data (black), along with the photospheric template (gray), which is scaled using the optical veiling derived from VLT spectra listed in Table 2. The single model with the highest likelihood is shown in red. The median model parameter values and their associated 1σ uncertainties are listed in Tables 3 and 5. The best-fit model is a combination of the accretion shock model (consisting of the three columns with energy fluxes of 1×10^{10}, 1×10^{11}, and 1×10^{12} erg s^{-1} cm^{-2}—cyan, sea-green, and brown dotted lines, respectively—with filling factors as indicated in the legend) and the DIAD model (consisting of the emission from the inner disk wall; lime-green dashed line). Residuals are shown in the bottom panel of each figure. Emission lines were excluded from the fit, and regions significantly affected by telluric absorption were excluded from both the observed spectra and model fitting; this produces the gaps seen in the residual plots. (a) The unscaled X-Shooter spectrum of CVSO 109 is shown in light gray. (b) The X-Shooter data for CVSO 165 are unresolved, so the NIR spectra have been scaled to align with the HST continuum of each component. This is just an approximation given that the two components have different spectral types. The X-Shooter spectrum of CVSO 176 has been scaled up to the HST continuum by a factor of 1.75 to account for the discontinuity between the continua, which is likely due to variability given that the observations were ∼65 hr apart. The unscaled X-Shooter spectra are shown in light gray.

(The data used to create this figure are available.)

V-band extinction A_V as a free parameter in the Markov Chain Monte Carlo (MCMC) fitting process and then calculate the stellar radius $R_\star$ from the fluxes of the dereddened CTTS spectrum and its associated X-shooter WTTS template scaled by the measured veiling. For details regarding the updates applied to the model, see Robinson & Espaillat (2019).

The complete shock model is composed of a WTTS template photosphere $F_{\rm phot}(\lambda)$ scaled to the veiling measured by Manara et al. (2021a), r_{λ_0} (shown in Table 2), plus three accretion columns of low, medium, and high flux densities ($\mathcal{F}=1\times10^{10}$, 1×10^{11}, and 1×10^{12} erg s^{-1} cm^{-2}, respectively). The emission from these columns is scaled by the stellar radius $R_\star$,

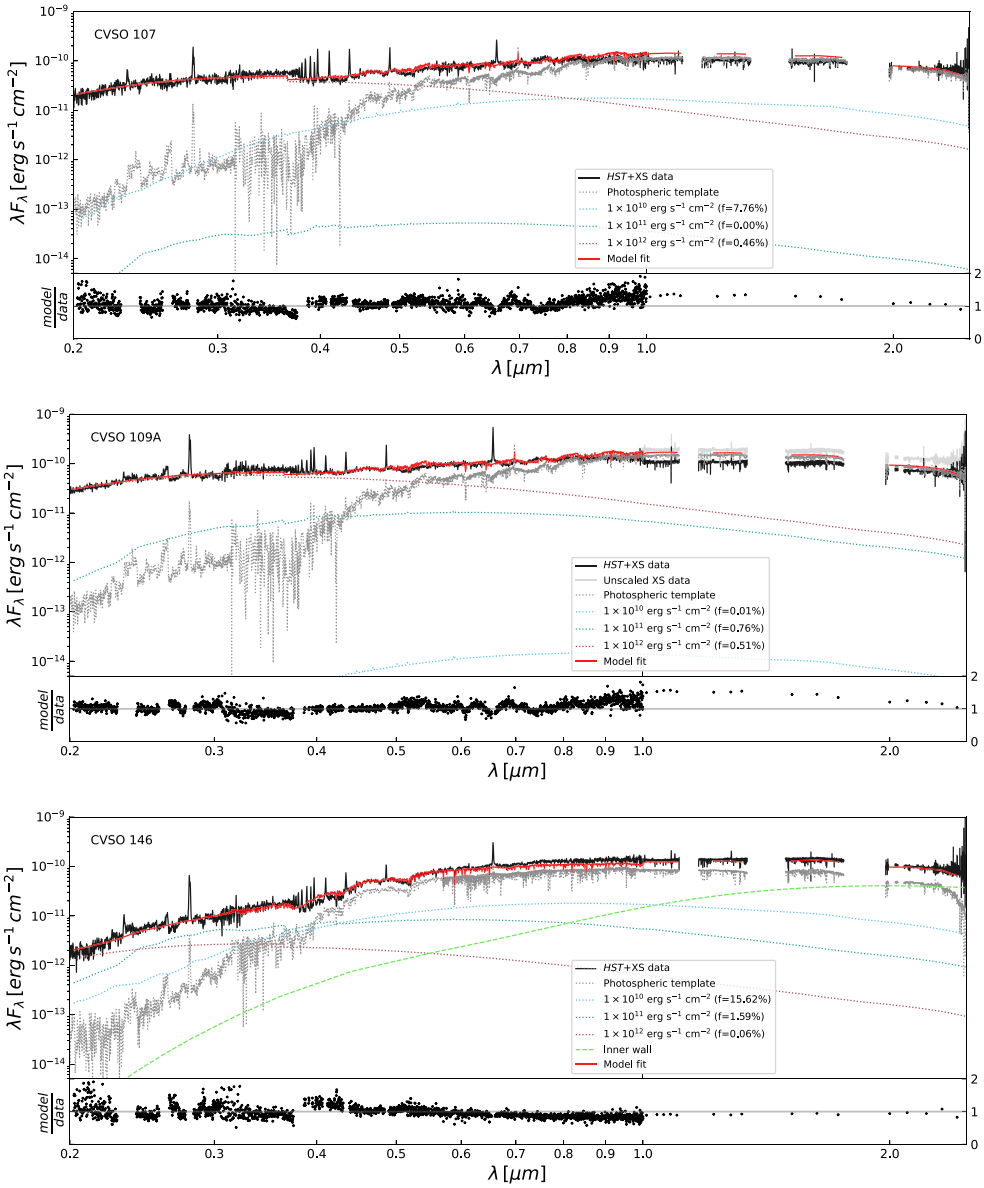

Figure 1. (Continued.)

the distance d, and filling factors f, which represent the fraction of the stellar surface that is covered by each accretion column. Thus, the total dereddened model flux is given by

$$F_{\rm tot}(\lambda) = 10^{0.4A_{\lambda_0}}\left[\frac{F_{\rm obs}(\lambda_0)}{F_{\rm phot}(\lambda_0)}\frac{F_{\rm phot}(\lambda)}{1+r_{\lambda_0}}\right] + \left(\frac{R_\star}{d}\right)^2\sum_i^n f_i\mathcal{F}_i(\lambda), \quad (1)$$

where A_{λ_0} is the extinction as described in Sections 2.2 and 2.3, $F_{\rm phot}(\lambda)$ is the WTTS template photosphere scaled by $F_{\rm obs}(\lambda_0)/F_{\rm phot}(\lambda_0)$ to the observed STIS spectrum at λ_0, n sums over the three accretion columns of different energy-flux densities, f_i are the filling factors associated with each accretion column, and $\mathcal{F}_i$ are the accretion shock spectra calculated as the sum of the emission from the heated photosphere and the preshock region of the system for each accretion column.

Equation (1) is fit to the HST continuum (with emission lines masked out) between 2000 and 10000 Å for each object using an MCMC with 2000 steps, 100 walkers, and a burn-in of 550. A_V has a top-hat prior ranging between 0 and 2 on account of the low extinction reported for Orion OB1 (median $A_V = 0.65$ mag; Briceño et al. 2019), and the sum of the filling factors is restricted between 0% and 40% of the stellar surface, as modeling has demonstrated that the footprint of the accretion column can produce detectable emission that covers up to 39% of the TTS surface (Ingleby et al. 2013, 2014; Robinson & Espaillat 2019). Once the best-fit model is obtained, the average temperature of the shock ($T_{\rm shock}$) is calculated by fitting blackbody curves to the three

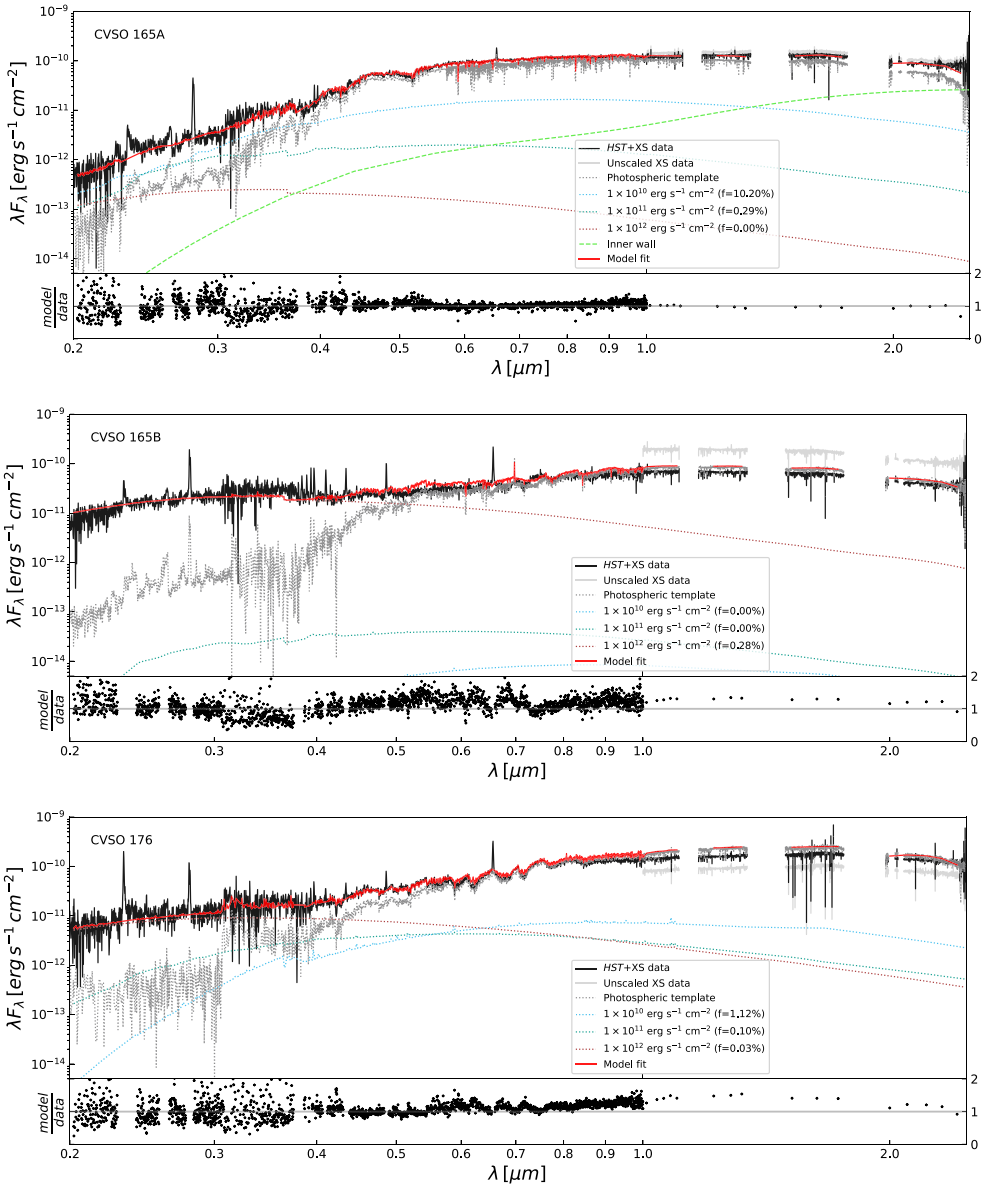

Figure 1. (Continued.)

columns' spectra and then weighting each column's associated accretion luminosity by its fractional filling factor according to

$$T_{\rm shock} = \left[\frac{f_{1E10}}{f_{\rm tot}} T_{1E10}^4 + \frac{f_{1E11}}{f_{\rm tot}} T_{1E11}^4 + \frac{f_{1E12}}{f_{\rm tot}} T_{1E12}^4 \right]^{\frac{1}{4}}. \quad (2)$$

The blackbody given by $T_{\rm shock}$ is an important input to the inner disk wall model, as both the stellar and the accretion luminosities irradiate the wall.

3.2. D'Alessio Irradiated Accretion Disk Model

We also model the protoplanetary disk's frontally illuminated inner dust wall, which is located at the dust sublimation radius, using the DIAD radiative transfer models (D'Alessio et al. 1998, 1999, 2001, 2004, 2005, 2006). The inner dust wall begins contributing significantly at 1 μm, after which the total model consists primarily of emission from the photosphere and the disk, with nonzero but less significant emission from the accretion columns at these longer wavelengths. Because our data extend only to 2.4 μm, our model includes only the inner wall, not the disk behind it.

For details regarding the DIAD model used here, see the ODYSSEUS I paper (Espaillat et al. 2022, Section 6.1.2). In short, we model the inner dust wall assuming a fractional abundance of graphite and pyroxene-type silicates of 0.0025 and 0.004, respectively, in accordance with the Draine & Lee (1984) model for the diffuse ISM. The magnesium-to-iron ratio, Mg/(Mg+Fe), is assumed to be 0.8, and we take the associated optical constants from Dorschner et al. (1995). The grains are spherical with a size distribution that scales as a^{-p} between grain radii of $a_{\rm min}$ and $a_{\rm max}$ and p of 3.5 (Mathis et al. 1977). The minimum grain size is held at 0.005 μm. Since the NIR spectra do not extend to 10 μm, we cannot confidently constrain the 10 μm silicate feature. Instead, we assume an $a_{\rm max}$ of 10 μm because Maucó et al. (2018) fit the 10 μm silicate

feature well with this value for the three objects from this analysis that were included in their study (CVSO 104, CVSO 107, and CVSO 109). The wall is illuminated by the stellar luminosity and the accretion luminosity, which is given by the $T_{\rm shock}$ derived for each target from its best-fit accretion shock model.

To obtain the best fit to the SED of each target, we adjust the height of the inner wall ($z_{\rm wall}$) between 0.5 and 20 gas scale heights (H), noting that the larger values of $z_{\rm wall}$ are indicative of excess emission likely originating from an optically thin dust cavity in a pre-transitional disk for which we do not account in this model (Maucó et al. 2018). We adjust the temperature of the optically thin wall atmosphere ($T_{\rm wall}$) between 1200 and 1800 K. Disk inclination i is estimated as described in Section 3.3.

Note that in the case of a vertical wall the inner disk wall height is degenerate with the inclination of the system. Since these disks are unresolved, we cannot distinguish between a high wall and a highly inclined viewing angle (we receive maximum wall emission from a disk inclined at 60°–80°; see Dullemond et al. 2001; Calvet et al. 2005).

The radius in the disk at which the wall is located ($R_{\rm wall}$) is derived using the best-fitting $T_{\rm wall}$ following

$$R_{\rm wall} \sim \left[\frac{(L_{*}+L_{\rm acc})}{16\pi\sigma_R}\left(2+\frac{\kappa_s}{\kappa_d}\right)\right]^{1/2}\frac{1}{T_{\rm wall}^2}, \quad (3)$$

which assumes that the thickness of the atmosphere is negligible compared to the radius (Muzerolle et al. 2003; D'Alessio et al. 2004), where σ_R is the Stefan–Boltzmann constant; κ_s and κ_d are the mean opacities to the incident and local radiation, respectively; $L_\star$ is the stellar luminosity; and $L_{\rm acc}$ is the luminosity of the stellar accretion shock as given by the output accretion rate ($\dot{M}$) and $R_\star$ of the multicolumn accretion shock model described in Section 3.1, with

$$L_{\rm acc} = (1 - 1/R_i)(GM_\star\dot{M}/R_\star). \quad (4)$$

As described in Section 3.1, R_i is taken to be 2.3 $R_\star$ for CVSO 109A and 5 $R_\star$ for all other targets. Disk models with $R_{\rm wall}$ located at the dust sublimation radius predict values of $R_{\rm wall}$ between 0.07 and 0.54 au, with stronger accretors having larger values of $R_{\rm wall}$ as indicated by Equation (3) (Muzerolle et al. 2003).

3.3. Inclinations

We infer the inclinations of our targets by estimating their stellar rotation periods from their TESS light curves and taking measurements of $v \sin i$ from Manara et al. (2021a) and Kounkel et al. (2019). Temporal analysis of the light curves uses the Scargle periodogram analysis (Scargle 1982; Horne & Baliunas 1986) as implemented in IDL.[25] We look for peaks in the power spectral density (PSD) between 1 and 10 days in excess of a 99% confidence level.

When power is found, we fold the data on the periods that show significant power. To minimize long-term secular variability, we construct a running mean of width 1.5 times the period and subtract that from the light curve prior to folding. We bin the data into 20 phase bins, setting the uncertainty in each phase bin to the variance in that bin, and test the binned light curve against the null hypothesis.

We also examine the autocorrelation of the light curve. The width of the correlation peak is proportional to the duration of the typical features contributing to the variations. We also consider the positive and negative excursions in the light curve separately: positive excursions may be due to bright patches on the photosphere; negative excursions may be due to occultations of the surface by circumstellar material, or by starspots. To define positive and negative excursions, we detrend the light curve with a polynomial fit (third to sixth order, depending on the number of points) and retain only those points above or below the trend. Brief discussions of the individual targets can be found in Appendix B.

[25] Jörn Wilms 2005: http://astro.uni-tuebingen.de/software/idl/aitlib/timing/scargle.html.

4. Analysis and Results

Figure 1 shows the best fits of the accretion shock and accretion disk models to the full NUV–NIR spectra of the nine CTTSs analyzed here. Table 3 lists the accretion model parameters associated with each fit, Table 4 gives our derived stellar periods and inclinations, and Table 5 lists the disk model parameters associated with each fit. Using our accretion shock model, we derive V-band extinction, stellar radius, accretion rate, and accretion column structure for each target.

Our results indicate that accretion remains strong in TTSs longer than originally expected. Hartmann et al. (2016) predict an accretion rate on the order of $3 \times 10^{-9}\ M_\odot\ {\rm yr}^{-1}$ for a $0.7\ M_\odot$ star of 5 Myr (the median age of the Orion OB1b region). However, Ingleby et al. (2014) measured accretion rates on the order of $1 \times 10^{-8}\ M_\odot\ {\rm yr}^{-1}$ for CVSO 58, CVSO 90, and CVSO 109. Similarly, our derived accretion rates are in the range of $(0.5\text{–}17.2) \times 10^{-8}\ M_\odot\ {\rm yr}^{-1}$, with a median value of $1.2 \times 10^{-8}\ M_\odot\ {\rm yr}^{-1}$. These accretion rates are comparable to those of the 1–2 Myr regions Taurus and Chamaeleon I (Ingleby et al. 2013). These high accretion rates produce associated accretion luminosities that range from 0.07 to $1.96\ L_\star$, with a median accretion luminosity of $0.25\ L_\star$. Given that the accretion luminosities are comparable to the stellar luminosities for these targets, the accretion rates from the accretion shock model are important inputs to the inner disk wall model.

The average accretion shock temperatures range from 4800 to 10,542 K, in agreement with the range predicted by Calvet & Gullbring (1998). With a mean temperature of 6511 K, these targets have $T_{\rm shock}$ notably lower than the typically assumed temperature of 8000–10,000 K for a single accretion column (e.g., D'Alessio et al. 1998; Fischer et al. 2011). The average temperatures of the three accretion columns are 4274 K for the low flux density column, 6695 K for the medium flux density column, and 10,786 K for the high flux density column. See Table 7 in Appendix C for the best-fit temperatures for each column of each target.

We are able to attain satisfactory fits to the NIR excesses of five targets, though there are a number of cases in which the photosphere goes above the data around 1 μm and thus forces the total model fit to be above the data (CVSO 58, CVSO 104, CVSO 107, CVSO 109A, CVSO 165B, and CVSO 176). In the cases of CVSO 107, CVSO 109A, CVSO 165B, and CVSO 176, there is no clear NIR excess above the photospheric and accretion shock emission, so no inner disk wall is fitted to these targets. This may result from variability in the veiling, which dictates the scaling of the WTTS photospheric template. This will be examined further in future work.

Table 3
Best-fit Accretion Shock Model Parameters of Orion OB1 CTTSs

Object	A_V	$R_\star$	$L_\star$	$L_{\rm acc}$	$\dot{M}$ (10^{-8}	f_{1E10}	f_{1E11}	f_{1E12}	$T_{\rm shock}$
	(mag)	($R_\odot$)	($L_\odot$)	($L_\odot$)	$M_\odot$ yr^{-1})	(fraction of stellar surface covered)			(K)
CVSO 58	$1.39^{+0.04}_{-0.04}$	$1.05^{+0.07}_{-0.07}$	0.25 ± 0.03	$0.202^{+0.011}_{-0.011}$	$1.03^{+0.05}_{-0.06}$	$0.231^{+0.010}_{-0.022}$	$0.00020^{+0.0017}_{-0.00013}$	$0.0092^{+0.0007}_{-0.0007}$	5493 ± 96
CVSO 90	$0.92^{+0.03}_{-0.30}$	$0.84^{+0.09}_{-0.09}$	0.12 ± 0.03	$0.234^{+0.011}_{-0.08}$	$1.25^{+0.06}_{-0.4}$	$0.053^{+0.016}_{-0.03}$	$0.00031^{+0.024}_{-0.00023}$	$0.0202^{+0.0011}_{-0.010}$	7975 ± 1105
CVSO 104	$0.05^{+0.05}_{-0.03}$	$1.64^{+0.13}_{-0.12}$	0.36 ± 0.06	$0.0655^{+0.003}_{-0.0021}$	$1.14^{+0.05}_{-0.04}$	$0.0304^{+0.0027}_{-0.004}$	$0.0074^{+0.0005}_{-0.0004}$	$0.00049^{+0.00006}_{-0.00003}$	5239 ± 105
CVSO 107	$1.16^{+0.03}_{-0.05}$	$1.97^{+0.15}_{-0.15}$	0.66 ± 0.10	$0.331^{+0.012}_{-0.021}$	$4.84^{+0.17}_{-0.3}$	$0.076^{+0.004}_{-0.007}$	$0.00015^{+0.0027}_{-0.00008}$	$0.00456^{+0.00024}_{-0.0004}$	5656 ± 128
CVSO 109A	$0.83^{+0.04}_{-0.32}$	$2.55^{+0.20}_{-0.20}$	1.18 ± 0.19	$0.61^{+0.04}_{-0.23}$	$17.2^{+1.0}_{-7}$	$0.0006^{+0.011}_{-0.0005}$	$0.0073^{+0.0026}_{-0.0021}$	$0.0051^{+0.0005}_{-0.0026}$	8877 ± 1910
CVSO 146	$0.28^{+0.03}_{-0.02}$	$1.25^{+0.09}_{-0.09}$	0.37 ± 0.05	$0.0926^{+0.003}_{-0.0027}$	$0.530^{+0.017}_{-0.015}$	$0.155^{+0.005}_{-0.006}$	$0.0159^{+0.0011}_{-0.0010}$	$0.00058^{+0.00005}_{-0.00004}$	4975 ± 27
CVSO 165A	$0.33^{+0.02}_{-0.02}$	$1.69^{+0.20}_{-0.20}$	0.56 ± 0.13	$0.0617^{+0.0017}_{-0.0015}$	$0.708^{+0.020}_{-0.017}$	$0.1020^{+0.0024}_{-0.003}$	$0.00287^{+0.0004}_{-0.00028}$	$0.0000485^{+0.000007}_{-0.0000023}$	4800 ± 14
CVSO 165B	$1.23^{+0.02}_{-0.02}$	$2.00^{+0.25}_{-0.25}$	1.14 ± 0.29	$0.176^{+0.005}_{-0.006}$	$1.65^{+0.05}_{-0.06}$	$0.00013^{+0.0004}_{-0.00007}$	$0.00009^{+0.00015}_{-0.00003}$	$0.00275^{+0.00008}_{-0.00012}$	10542 ± 343
CVSO 176	$1.44^{+0.03}_{-0.03}$	$3.26^{+0.31}_{-0.31}$	1.08 ± 0.21	$0.0815^{+0.0023}_{-0.0020}$	$4.18^{+0.12}_{-0.10}$	$0.0108^{+0.0019}_{-0.004}$	$0.00106^{+0.00026}_{-0.00020}$	$0.000267^{+0.000017}_{-0.000015}$	5043 ± 254

Note. Best-fit accretion shock model parameters for each CTTS. To calculate the models, the stellar mass, distance, temperature, and veiling are adopted as given in Table 2. R_i is taken to be 5 $R_\star$ for all targets except CVSO 109A, which has $R_i = 2.3$ $R_\star$ as described in Section 3.1. For the best-fit temperatures of individual accretion columns, see Table 7 in Appendix C.

(This table is available in machine-readable form.)

Table 4
Periods and Inclinations of Orion OB1 CTTSs

Object	$v \sin i$ (km s^{-1})	Period (days)	v (km s^{-1})	i (deg)
CVSO 58	17.9 ± 1.3	5.7	9.3 ± 0.5	⋯
CVSO 90	8.3 ± 1.6	5.1	8.3 ± 0.9	⋯
CVSO 104	7.5 ± 1.0	4.7	17.7 ± 1.3	25.1 ± 4.1
CVSO 107	5.9 ± 0.9	6.4	15.6 ± 0.9	22.3 ± 3.9
CVSO 109A	3.2 ± 0.9	6.5	19.8 ± 1.2	9.3 ± 2.7
CVSO 146	5.0 ± 0.8	5.5	11.5 ± 0.7	25.8 ± 4.8
CVSO 165A	15.4 ± 0.9	4.3	19.9 ± 1.4	50.8 ± 6.5
CVSO 165B	15.4 ± 0.9	4.3	23.5 ± 1.9	40.9 ± 4.9
CVSO 176	18.4 ± 1.2	7.1	23.2 ± 1.9	52.4 ± 7.8

Note. Calculated inclinations i for our targets. $v \sin i$ comes from the VLT modeling that produced the veilings used in this paper (Manara et al. 2021a) for all targets except CVSO 90, which takes $v \sin i$ from Kounkel et al. (2019). Stellar rotational velocities v are calculated using the radii we derive here. The derived v for CVSO 58 is smaller than its $v \sin i$, and the calculated i for CVSO 90 has an error of almost $\pm 180°$; thus, inclination is assumed to be a standard 60° for these targets, corresponding to $\cos(i) = 0.5$.

(This table is available in machine-readable form.)

Table 5
Best-fit Accretion Disk Model Parameters of Orion OB1 CTTSs

Object	$z_{\rm wall}$ (H)	$T_{\rm wall}$ (K)	$R_{\rm wall}$ (au)
CVSO 58	5	1200	0.10
CVSO 90	5.5	1600	0.06
CVSO 104	5.5	1200	0.07
CVSO 146	18	1800	0.05
CVSO 165A	8	1400	0.07

Note. Best-fit parameters for the the accretion disk models given input parameters as shown in Tables 2 and 3. We adopt $a_{\rm min} = 0.005$ μm, $a_{\rm max}$= 10 μm, and $p = 3.5$. Disk inclinations i are taken from Table 4.

The lack of NUV spectra of WTTS templates with the same spectral subtype as some of the CTTSs may produce scaling that results in mismatches in the NIR. Four out of the five targets that are fit with an inner wall require a wall height in excess of 5 gas scale heights to produce enough emission to account for the excess. These targets are likely pre-transitional disks, which have extra emission from an optically thin dust component in their inner disk cavities (Maucó et al. 2018). Our future work will examine whether this additional component produces a better fit to the data. Additionally, we will examine whether using a lower magnesium-to-iron ratio can account for some of the excess, as was found by McClure et al. (2013).

4.1. Uncertainties

The average accretion shock model uncertainty, quantified by an MCMC nuisance parameter, is 14%. This statistical goodness of fit is a lower limit to the actual uncertainty, as it does not take the uncertainties of the input parameters, the photospheric templates, or the extinction curve into account. When accretion rates are calculated considering the uncertainties in $R_\star$ and the filling factors, and assuming an uncertainty of 2 $R_\star$ for the magnetospheric truncation radius R_i, the median percent error increases from 4% to 32%.

Uncertainties in our derived stellar radii take into account the error in the data fluxes, CTTS distance, veiling, visual extinction, and an assumed 10% error in the WTTS template fluxes. Our estimates have an average percent error of 8%. The updated luminosity measurements included in Table 3 propagate our derived error in $R_\star$, but no uncertainty is assumed for the stellar temperature. The uncertainties in the average shock temperature are dominated by the errors in the filling factors. Since the errors are often asymmetric, the larger of the upper and lower uncertainties is taken as the error in propagation.

A significant source of systematic uncertainty comes from the availability and scaling of the WTTS photospheric templates. There are seven total WTTS templates with NUV spectra available between SpTs K5 and M2, and there are no templates of type K6 or M0. All CTTSs studied here are fit with a template within 1.5 subtypes of their own spectral classification, but even this difference in spectral type introduces some amount of error. Fitting each target CTTS with the next-closest template on either side, when available, changes the best-fit visual extinction by 0.37 mag on average.

Table 6
Literature Comparison

Object	$\dot{M}_{\rm C05}$ ($\times10^{-8}$)	$A_{V,\rm C05}$ (mag)	$\dot{M}_{\rm I14}$ ($\times10^{-8}$)	$A_{V,\rm I14}$ (mag)	$\dot{M}_{\rm M18}$ ($\times10^{-8}$)	$A_{V,\rm M18}$ (mag)	$\dot{M}_{\rm M21}$ ($\times10^{-8}$)	$A_{V,\rm M21}$ (mag)	BC	$\dot{M}_{\rm P22}$ ($\times10^{-8}$)	$A_{V,\rm P22}$ (mag)
CVSO 58	0.45	0.12	1.60	0.8 ± 0.5	⋯	⋯	0.43	0.8		$1.03^{+0.06}_{-0.06}$	$1.39^{+0.04}_{-0.04}$
CVSO 90	1.77	0.00	1.00	0.0 ± 0.4	⋯	⋯	0.25	0.1		$1.25^{+0.05}_{-0.5}$	$0.92^{+0.03}_{-0.30}$
CVSO 104	0.75	0.00	⋯	⋯	0.56	0.1	0.32	0.2		$1.14^{+0.06}_{-0.04}$	$0.05^{+0.05}_{-0.03}$
CVSO 107	1.09	0.32	0.25	0.7 ± 0.4	0.29	0.4	5.01	0.3		$4.83^{+0.19}_{-0.29}$	$1.16^{+0.03}_{-0.05}$
CVSO 109	2.52	0.00	3.00	0.8 ± 0.5	0.67	0.0	3.24	0.1	A	$17.2^{+1.0}_{-6}$	$0.83^{+0.04}_{-0.32}$
CVSO 146	0.81	0.37	⋯	⋯	⋯	⋯	0.27	0.6		$0.529^{+0.016}_{-0.015}$	$0.28^{+0.03}_{-0.02}$
CVSO 165	0.37	0.00	⋯	⋯	⋯	⋯	0.08	0.2	A	$0.708^{+0.021}_{-0.017}$	$0.33^{+0.02}_{-0.02}$
	⋯	⋯	⋯	⋯	⋯	⋯	⋯	⋯	B	$1.65^{+0.05}_{-0.06}$	$1.23^{+0.02}_{-0.02}$
CVSO 176	0.43	0.00	⋯	⋯	⋯	⋯	1.45	1		$4.19^{+0.12}_{-0.11}$	$1.44^{+0.03}_{-0.03}$

Note. Comparison between the accretion rates and visual extinctions derived here and those derived by Calvet et al. (2005; C05), Ingleby et al. (2014; I14), Maucó et al. (2018; M18), and Manara et al. (2021a; M21). For the binary targets that are resolved in this study, the BC column indicates which binary component is being referenced.

Once a template is chosen, it must be scaled to the data by the veiling measurement, which has its own variability and uncertainty. Three measurements of veiling, each separated by a day, were available for all targets except CVSO 90 and CVSO 104. The measured veiling for a given target varied, on average, by a factor of 1.6 across the three epochs. By choosing the epoch closest in time to the HST observations, we minimize the influence of veiling variability, but it cannot be completely removed.

Our derivations of inclinations are rough estimates given that the stellar rotation periods in the TESS data can easily be obscured by other processes, such as occultation dips and discrete accretion events. Uncertainties have not been determined for the period measurements, so the quoted uncertainties in inclinations come from errors in $v \sin i$ and $R_\star$. We note that if the inclination estimates are wrong, the only parameter that would be affected is the height of the inner disk wall $z_{\rm wall}$.

5. Discussion

In Section 5.1, we place our results in the context of previous studies. In Section 5.2, we examine the significance of the choice of extinction law and the wavelength range of data available.

5.1. Comparison to Previous Results

Robinson & Espaillat (2019) applied the multicolumn accretion shock model from Ingleby et al. (2013) to multiepoch observations of five CTTSs and found that mass accretion rates vary with a spread of a factor of ∼2 for a given object. Similarly, Venuti et al. (2014) found that the accretion rate for a given object has a spread of 0.5 dex (a factor of ∼3) from studying about 200 CTTSs in NGC 2264. Rather than merely representing this intrinsic variability, the best-fit values for accretion rate and visual extinction presented in this work are systematically higher than those found by previous studies of objects in this sample (Calvet et al. 2005; Ingleby et al. 2014; Maucó et al. 2018; Manara et al. 2021a). See Table 6 for the individual values found by each work.

Calvet et al. (2005) modeled all CTTSs analyzed here (though their observations of binaries CVSO 109 and CVSO 165 were unresolved), obtaining accretion rates for each using photometric excesses in *U–B* and *U–V*. They cite an overall uncertainty of a factor of 3 for each measured accretion rate, with the largest contribution coming from uncertainty in the extinction. They calculate A_V from the $V - I_C$ color using the Cardelli et al. (1989) extinction law with $R_V = 3.1$. The accretion rates measured here are 0.6–9.7 times those presented in Calvet et al. (2005), with a median ratio of 2.3. This cannot be attributed to different flux levels, as all of our observed *U–V* colors are redder than those presented in Calvet et al. (2005). Additionally, our measured extinctions are systematically larger than those of Calvet et al. (2005), with a median difference of 0.8 mag. Because our accretion rates are systematically higher, it is likely that the different accretion rates result from systematic effects in the different modeling techniques and adopted extinctions rather than solely from true variability.

The closest analog to our modeling technique is that of Ingleby et al. (2014), who modeled CVSO 58, CVSO 90, CVSO 107, and the unresolved CVSO 109 system. They used the veiling at *V* and *I* to estimate extinction by comparing the observed photospheric $V–I_C$ colors to the standard colors in Kenyon & Hartmann (1995). They note that their inferred *V*-band extinctions would have decreased by 0.2–0.4 mag had they used the colors of Pecaut & Mamajek (2013), and this in turn would decrease their $\dot{M}$ values by a factor of 1.82.4. They then deredden their data using the Whittet et al. (2004) law toward HD 29647, as we do here. The MagE and MIKE spectra they used for these four targets covered only 3400–9000 Å, so their fitting does not include the NUV.

Ingleby et al. (2014) thus fit the excess shock emission beyond the Balmer jump using a five-column accretion shock model also based on Calvet & Gullbring (1998) (the three columns used here plus two intermediate columns). However, instead of using the standard accretion shock model, they found that they needed to increase the low-density preshock emission by up to a factor of five to accurately reproduce the bluest regions of the excess emission spectra. This likely explains why the structure of their accretion columns, specifically the area they cover, is notably different from this work. Some of our model fits show a trend of underestimating the flux near the Balmer jump; future work will examine whether increasing this preshock emission produces a better fit to the data, or whether this is merely an effect of Balmer-line crowding that is not accounted for by our continuum model.

The ratios of our accretion rates to those of Ingleby et al. (2014) are 0.7 (CVSO 58), 1.2 (CVSO 90), 19.3 (CVSO 107), and 5.7 (CVSO 109). Note that had they used the same spectral

type–color conversion as we did (Pecaut & Mamajek 2013), these ratios would have been higher as described above. The differences in our derived accretion rates correspond to the differences in U- and V-band magnitudes between our respective observations. CVSO 58 was dimmer in both bands in our epoch of observations ($\Delta U = 0.70$ mag, $\Delta V = 0.38$ mag), and we find a lower accretion rate. The other three CTTSs were brighter in both bands in our epoch—CVSO 90 ($\Delta U = -0.48$ mag, $\Delta V = -0.53$ mag), CVSO 107 ($\Delta U = -0.61$) mag, $\Delta V = -0.04$ mag), and CVSO 109A ($\Delta U = -1.11$ mag, $\Delta V = -0.09$ mag)—and we found higher accretion rates for these. The greatest increase in U-band belongs to CVSO 109A, which is consistent with the TESS light curve that shows that our HST observation occurred near a local maximum in CVSO 109's light curve (Espaillat et al. 2022). These magnitudes come from observed, rather than dereddened, data, so differences in our treatments of extinction have no effect. Thus, our accretion rates are in broad agreement with those of Ingleby et al. (2014).

Maucó et al. (2018) estimated accretion rates for CVSO 104, CVSO 107, and the unresolved CVSO 109 system using the Hα–$\dot{M}$ relation found for Taurus CTTSs by Ingleby et al. (2013): $\log(\dot{M}) = 1.1(\pm0.3)\log(L_{\mathrm{H}\alpha}) - 5.5(\pm0.8)$, where the value of the Hα line luminosity was estimated as its equivalent width times the continuum flux. Espaillat et al. (2022) found that for CVSO 109 this method produces a lower accretion rate than do the accretion shock models. This is what we find here, as the ratios of our accretion rates to theirs are 2.0 (CVSO 104), 16.7 (CVSO 107), and 25.7 (CVSO 109). The discrepancy may result from (1) the small number of sources used to determine this relation (10 CTTSs) or (2) the assumption of a uniform distance for all Taurus CTTSs (140 pc) in the determination of $L_{\mathrm{H}\alpha}$.

Manara et al. (2021a) analyzed X-Shooter spectra of all of the ULLYSES Orion targets, using a hydrogen slab model to obtain their accretion properties. They fit for A_V using the Cardelli et al. (1989) extinction law. X-Shooter spectra are available only beyond 3000 Å, so the NUV is not included in their analysis. Our multicolumn accretion shock model finds higher accretion rates for all targets except CVSO 107, which has the highest accretion rate in the analysis of Manara et al. (2021a). The median ratio of our accretion rates to theirs is 3.5.

Six of our CTTS targets have stellar radii from Manara et al. (2021a) included in Table 2. There are no individual uncertainties available for the Manara et al. (2021a) spectral types and luminosities, but previous work using their method of determining stellar radii showed that objects with spectral types earlier than M4.5 have percent errors less than 25% (Alcalá et al. 2017). Assuming a percentage error of 25% for the radii calculated from the Manara et al. (2021a) spectral types and luminosities, we find that our best-fit radii for CVSO 58, CVSO 90, and CVSO 104 are consistent within the errors; those fit for CVSO 107 and CVSO 176 are larger by a factor of 1.4 and 1.8, respectively; and that fit for CVSO 146 is lower by a factor of 1.5.

The systematically higher accretion rates presented in this work can in large part be attributed to (a) our use of the accretion shock model as opposed to Hα luminosity or an isothermal hydrogen slab model and (b) the larger NUV wavelength coverage of these data, as the NUV is the most important region for constraining the highest energy-flux density accretion column. The latter has the important implication that all ground-based measurements of CTTS accretion rates may be underestimated. Since HST has a finite lifetime, future work should examine whether a correction factor can be determined to account for the systematic underestimation of accretion rates caused by the lack of NUV coverage.

5.2. Extinction Law

When modeling NUV observations of CTTSs, the choice of extinction law is incredibly important because of the strong attenuation by grains at UV wavelengths and the constraint imposed by the 2175 Å bump. If a law produced for the general ISM is used, such as Cardelli et al. (1989) or Fitzpatrick et al. (2019), the absorption bump feature is strong and will bias results toward lower values of A_V. If, by contrast, the Whittet et al. (2004) law toward HD 29647 (which is embedded in Taurus) is used, the absorption feature is much less pronounced and the fitted A_V will be higher.

No single interstellar extinction law can describe all star-forming regions equally well. This is supported by the finding that Taurus and Ophiuchus exhibit very different UV extinction functions, which Whittet et al. (2004) suggest is likely caused by their different populations of massive stars. Ophiuchus's significant population of OB stars produce radiation that maintains the strength of the 2175 Å bump, so the Cardelli et al. (1989) law is better suited for use there than is the Whittet et al. (2004) law. Thus, NUV data for specific TTSs provide an important constraint on the characteristics of both the individual stars themselves and their surrounding environments. Data from HST are vital for probing the ISM of star-forming regions to distinguish between grain populations that significantly attenuate around 2175 Å and those that do not.

For these targets in Orion, the fits produced by the Whittet et al. (2004) law are better than those produced by the Cardelli et al. (1989) law, which overcorrects for the 2175 Å bump (see Figure 2). This indicates that Orion OB1b is likely more similar to Taurus than Ophiuchus in terms of its interstellar extinction function. This is supported by an analysis of the UV interstellar radiation field (ISRF) of the region. The Habing field parameter G_0 gives the ratio of the local field enhanced by a neighboring OB star to the typical ISRF (F_0) according to

$$G_0 = \frac{1}{F_0}\frac{L_{\mathrm{FUV}}}{4\pi r^2}, \tag{5}$$

where F_0 is assumed to be 1.6×10^{-3} erg s^{-1} cm^{-2} (Habing 1968), L_{FUV} is approximated as the OB star's luminosity, and r is the true distance between the OB star and the CTTS target of interest (Anderson et al. 2013; Maucó et al. 2016).

Liseau et al. (1999) found that the ρ Ophiuchi star-forming region has $G_0 = 20$–140. In contrast, G_0 values for our OB1b CTTS targets are much lower. Assuming that the seven most significant OB stars around Orion OB1b (ζ Ori, ϵ Ori, δ Ori, η Ori, 22 Ori, 25 Ori, and ψ^2 Ori) are all at the median OB1b distance of 400 pc, G_0 for our targets has a median value of 0.7 and a maximum value of 67. This, in combination with the low A_V of the region, demonstrates that although Orion OB1b is an OB region, its interstellar extinction function should align more with that of quiescent Taurus than that of hotter, dustier ρ Ophiuchi. This can in part explain the relatively high accretion rates of this region in spite of its intermediate age, as these disks have not been externally photoevaporated by an enhanced ISRF. This is also consistent with the disk models from Calvet et al. (2005), which could not reproduce the low long-wavelength

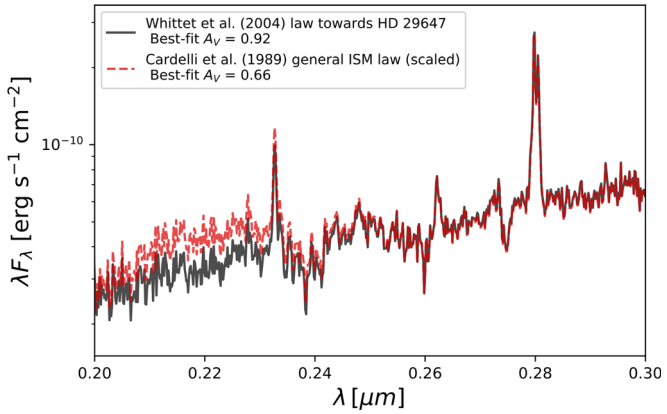

Figure 2. Spectra of CVSO 90 dereddened with the best-fit *V*-band extinction when modeled with the Whittet et al. (2004) law (black solid line) and Cardelli et al. (1989) law (red dashed line, shown scaled to the Whittet et al. 2004 law spectrum at 3000 Å). The overcorrected 2175 Å bump is apparent in the red curve.

IR fluxes observed in Orion OB1 using small outer disk radii consistent with external photoevaporation (∼30 au). Instead, they concluded that the disks must be flatter and have larger maximum grain sizes than those in Taurus ($a_{\rm max} = 1$ mm). For an analysis of the effect of an enhanced ISRF on circumstellar disk evolution, see Anderson et al. (2013).

The ULLYSES survey, which will provide over 80 custom-calibrated NUV spectra of CTTSs in nine star-forming regions, will allow us to examine the goodness of fit of different extinction laws in different environments. Beyond this, it would be ideal to attain extinction curves for all nearby star-forming regions rather than using either a general ISM curve or the curve calculated to the specific environment of Taurus.

6. Summary

1. Accretion rates for the nine CTTSs studied here are in the range of $(0.5 - 17.2) \times 10^{-8}\ M_\odot\ {\rm yr}^{-1}$, relatively high for the intermediate age of Orion OB1b.
2. Our accretion rates and *V*-band extinctions are systematically higher than those calculated from optical data in previous works, in large part due to our wavelength coverage that extends into the NUV.
3. The NIR excesses of the five targets in which an excess is present are fit with 1200–1800 K inner disk walls located at 0.05–0.10 au from the host stars.
4. The choice of extinction law significantly affects the calculated accretion rate and introduces uncertainty that is difficult to quantify. Our analysis indicates that the environment of Orion OB1b is more similar to quiescent Taurus than to hot ρ Ophiuchi. Ideally, extinction curves can be calculated for each star formation region in the near future.
5. This multicolumn shock and DIAD analysis will be applied to all nine star-forming regions being observed through ULLYSES, allowing us to extend the analysis across distinct stellar populations and search for correlations between accretion and disk properties in a larger sample. Additionally, it will be applied to the four CTTSs being monitored by the ULLYSES program (GM Aur, TW Hya, BP Tau, and RU Lup).

Support for this work comes from HST AR-16129, as well as NASA through grant No. AR 16129 from the Space Telescope Science Institute, which is operated by AURA, Inc., under NASA contract NAS 5-26555. This work benefited from discussions with the ODYSSEUS team (https://sites.bu.edu/odysseus/); see Espaillat et al. (2022) for an overview of the ODYSSEUS survey.

J.H. acknowledges support from CONACyT project No. 86372 and the UNAM-DGAPA-PAPIIT project IA102921. P.A., E.F., and Á.K. acknowledge support from the European Research Council (ERC) under the European Union's Horizon 2020 research and innovation programme under grant agreement No. 716155 (SACCRED). C.F.M. acknowledges funding by the European Union under the European Union's Horizon Europe Research & Innovation Programme 101039452 (WANDA). Views and opinions expressed are, however, those of the author(s) only and do not necessarily reflect those of the European Union or the European Research Council. Neither the European Union nor the granting authority can be held responsible for them. C.F.M., J.M.A, M.G., and E.F. acknowledge support from the project PRIN-INAF 2019 "Spectroscopically Tracing the Disk Dispersal Evolution." S.H.P.A. acknowledges support from CNPq, CAPES, and Fapemig.

Based on observations obtained with the NASA/ESA Hubble Space Telescope, retrieved from the Mikulski Archive for Space Telescopes (MAST) at the Space Telescope Science Institute (STScI). STScI is operated by the Association of Universities for Research in Astronomy, Inc., under NASA contract NAS 5-26555.

This paper utilizes the D'Alessio irradiated accretion disk (DIAD) code. We wish to recognize the work of Paola D'Alessio, who passed away in 2013. Her legacy and pioneering work live on through her substantial contributions to the field.

Appendix A
CVSO 17 and CVSO 36

As shown in Figure 3, we find that CVSO 17 and CVSO 36 show no significant UV continuum excess in their HST spectra that would indicate active accretion, which aligns with the analysis of their X-Shooter spectra by Manara et al. (2021a) and confirms their photometric characterization as WTTSs by Calvet et al. (2005). Additionally, an analysis of their far-UV spectra shows no fluorescent H_2 emission, which is a clear delineation between CTTSs and WTTSs (France et al. 2012; Alcalá et al. 2019).

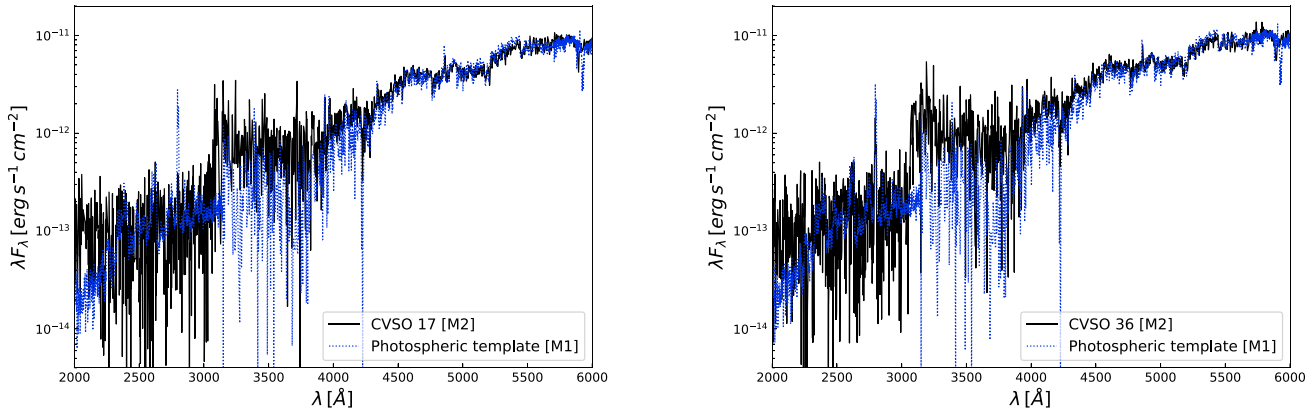

Figure 3. The photospheric template shown is the M1 WTTS TWA 7.

Appendix B
TESS Object Notes

CVSO 58: In Sector 6 there was significant power at 2.87 and 5.31 days. The 2.9-day period folds well, but the likelihood that the amplitude of the period is significant is only 0.12. In Sector 32 significant power exists at 6.45 and 1.41 days, but neither looks periodic after folding. The autocorrelation functions in both sectors show a peak near 5.7 days. This peak is strongest for the dips; during Sector 6, the positive excursions (brightenings) show a less well-defined peak at a period near 6 days.

CVSO 90: The Sector 6 PSD peaks at 3.15 days, but there is no significant period seen in the folded light curve. The Sector 32 PSD shows a strong and broad peak at 5.11 days. The folded light curve is not significant owing to lots of scatter in the half of the period dominated by deep dips. The autocorrelation function shows a peak at a lag of about 4.4 days for the absorption dips and a peak at a 5.7-day period for the brightenings.

CVSO 104: This star has a peak in the PSD near 4.7 days in each sector. It is not clear whether the light curve is dominated by bright or dark excursions. We do not attempt to fold the two sectors together because it it impossible to keep track of the phases over this time.

CVSO 107: The Sector 6 light curve is dominated by two deep dips spaced 12 days apart. The periodogram finds power at 6.3 days, or half that spacing. Power at the same period also dominates in Sector 32. The brightenings show a preferred lag of 6.5 days, while the dips lag at 7.7 days. There are three possible short flares of 2–3 hr duration in Sector 6.

CVSO 109: The two light curves look similar, with strongest power near 6 days (6.0 days in Sector 6, 6.6 days in Sector 32). After subtracting an 8-day running mean, the folded light curves look sinusoidal, with amplitudes of about 0.07 mag. The autocorrelation functions are broad, consistent with a sinusoidal modulation.

CVSO 146: This star is partially blended with the brighter A2 star HD 290671 in the TESS images (4.8-pixel separation). The A star has a low-amplitude 1.56-day period. There is power at about 9 days in each sector; there is additional power at 5.5 days in Sector 6 and 4.4 days in Sector 32. None of these appear periodic. The autocorrelation power in Sector 6 is strongest for the dips, at a period of 10–12 days; the brightenings show a correlation at 7–8 days; in Sector 32 both the brightenings and fadings show power near 5 days, with comparable peaks near 7 days (brightenings) and 8 days (fadings).

CVSO 165: TESS cannot resolve this pair. The periodograms at both epochs show strongest power at 4.3 days; in the latter half of Sector 32 there are two prominent (0.1 mag) dips, and possibly two others cut off, at this spacing, but that period is not obvious at other times. There is substructure in Sector 6, with the brightenings correlating with lags of 7.7 and 13 days and the fadings correlating at 8.8 days (twice the strongest period) and 11.6 days. In Sector 32 the brightenings and fadings correlate on the 4.3-day period.

CVSO 176: This was not observed by TESS in Sector 32. In Sector 6 the character is clearly that of a dipper, with fadings up to 0.2 mag. Despite the periodogram placing most of the power at 3.6 days, the autocorrelation shows the strongest peak at 7.3 days, in both brightenings and dips.

Appendix C
Accretion Column Temperatures and Mass Flux Rates

Blackbodies are individually fit to the three accretion column spectra of each target, and then a weighted average is taken by scaling the associated accretion luminosities by each column's fractional filling factor according to Equation (2). Table 7 shows the individual temperatures fit to each accretion column.

Table 8 shows the mass flux rates of the individual accretion columns for each target. We find no clear correlations between the column that contributes the most to the total mass flux and either the stellar mass or the total mass accretion rate. Our future analysis of the entire ULLYSES sample will allow us to expand this analysis and look for correlations with stellar age.

Table 7
Accretion Column Temperatures

Object	T_{1E10} (K)	T_{1E11} (K)	T_{1E12} (K)	T_{shock} (K)
CVSO 58	4422 ± 1	6880 ± 3	$10{,}916 \pm 3$	5493 ± 96
CVSO 90	4171 ± 2	6816 ± 3	$10{,}870 \pm 3$	7975 ± 1105
CVSO 104	4051 ± 2	6634 ± 3	$10{,}698 \pm 3$	5239 ± 105
CVSO 107	4187 ± 2	6696 ± 3	$10{,}679 \pm 3$	5656 ± 128
CVSO 109A	4255 ± 2	6506 ± 2	$10{,}714 \pm 2$	8877 ± 1910
CVSO 146	4459 ± 1	6871 ± 3	$10{,}973 \pm 3$	4975 ± 27
CVSO 165A	4675 ± 1	6853 ± 3	$10{,}760 \pm 3$	4800 ± 14
CVSO 165B	4309 ± 1	6690 ± 3	$10{,}729 \pm 3$	$10{,}542 \pm 343$
CVSO 176	3938 ± 2	6310 ± 1	$10{,}736 \pm 2$	5043 ± 254

Note. Best-fit temperatures for the three accretion columns and the resultant weighted-average temperature. Uncertainties on T_{1E10}, T_{1E11}, and T_{1E12} are one standard deviation on the temperature. The error on T_{shock} comes from the propagated accretion column temperature and filling factor uncertainties. Since the filling factor uncertainties are not symmetric, the larger of the two uncertainties is used in the error propagation.

(This table is available in machine-readable form.)

Table 8
Accretion Column Mass Flux Rates

Object	$M_\star/R_\star$ ($M_\odot/R_\odot$)	$\dot{M}_{1E10}$ ($10^{-8}\ M_\odot\ yr^{-1}$)	$\dot{M}_{1E11}$ ($10^{-8}\ M_\odot\ yr^{-1}$)	$\dot{M}_{1E12}$ ($10^{-8}\ M_\odot\ yr^{-1}$)	$\dot{M}_{tot}$ ($10^{-8}\ M_\odot\ yr^{-1}$)
CVSO 176	0.08	$0.93^{+0.17}_{-0.4}$	$0.92^{+0.22}_{-0.18}$	$2.31^{+0.15}_{-0.13}$	$4.18^{+0.11}_{-0.12}$
CVSO 104	0.23	$0.227^{+0.021}_{-0.03}$	$0.55^{+0.04}_{-0.03}$	$0.360^{+0.05}_{-0.022}$	$1.14^{+0.06}_{-0.03}$
CVSO 109A	0.20	$0.018^{+0.28}_{-0.015}$	$2.1^{+0.7}_{-0.6}$	$15.1^{+1.5}_{-5}$	$17.2^{+1.0}_{-4}$
CVSO 107	0.27	$0.69^{+0.04}_{-0.06}$	$0.012^{+0.23}_{-0.007}$	$4.11^{+0.23}_{-0.4}$	$4.83^{+0.19}_{-0.3}$
CVSO 165A	0.34	$0.531^{+0.012}_{-0.017}$	$0.150^{+0.020}_{-0.014}$	$0.0253^{+0.004}_{-0.0013}$	$0.708^{+0.020}_{-0.017}$
CVSO 90	0.74	$0.032^{+0.010}_{-0.019}$	$0.0018^{+0.16}_{-0.0014}$	$1.21^{+0.06}_{-0.6}$	$1.25^{+0.05}_{-0.4}$
CVSO 58	0.77	$0.206^{+0.009}_{-0.019}$	$0.0018^{+0.016}_{-0.0012}$	$0.82^{+0.06}_{-0.07}$	$1.03^{+0.06}_{-0.06}$
CVSO 165B	0.42	$0.0007^{+0.0026}_{-0.0004}$	$0.0053^{+0.010}_{-0.0020}$	$1.64^{+0.05}_{-0.07}$	$1.65^{+0.05}_{-0.07}$
CVSO 146	0.69	$0.220^{+0.007}_{-0.008}$	$0.226^{+0.015}_{-0.014}$	$0.082^{+0.007}_{-0.006}$	$0.529^{+0.018}_{-0.016}$

Note. Mass flux rates of individual accretion columns with targets listed in order of increasing stellar mass. There is no clear correlation between the column that dominates the mass flux and either the stellar mass or the total accretion rate.

(This table is available in machine-readable form.)

ORCID iDs

Caeley V. Pittman https://orcid.org/0000-0001-9301-6252
Catherine C. Espaillat https://orcid.org/0000-0001-9227-5949
Connor E. Robinson https://orcid.org/0000-0003-1639-510X
Thanawuth Thanathibodee https://orcid.org/0000-0003-4507-1710
Nuria Calvet https://orcid.org/0000-0002-3950-5386
John Wendeborn https://orcid.org/0000-0002-6808-4066
Jesus Hernández https://orcid.org/0000-0001-9797-5661
Carlo F. Manara https://orcid.org/0000-0003-3562-262X
Fred Walter https://orcid.org/0000-0001-7796-1756
Péter Ábrahám https://orcid.org/0000-0001-6015-646X
Juan M. Alcalá https://orcid.org/0000-0001-8657-095X
Sílvia H. P. Alencar https://orcid.org/0000-0002-5171-8376
Nicole Arulanantham https://orcid.org/0000-0003-2631-5265
Sylvie Cabrit https://orcid.org/0000-0002-1593-3693
Jochen Eislöffel https://orcid.org/0000-0001-6496-0252
Eleonora Fiorellino https://orcid.org/0000-0002-5261-6216
Kevin France https://orcid.org/0000-0002-1002-3674
Manuele Gangi https://orcid.org/0000-0002-8364-7795
Konstantin Grankin https://orcid.org/0000-0001-5707-8448
Gregory J. Herczeg https://orcid.org/0000-0002-7154-6065
Ágnes Kóspál https://orcid.org/0000-0001-7157-6275
Ignacio Mendigutía https://orcid.org/0000-0002-0233-5328
Javier Serna https://orcid.org/0000-0001-7351-6540
Laura Venuti https://orcid.org/0000-0002-4115-0318

References

Alcalá, J. M., Manara, C. F., France, K., et al. 2019, A&A, 629, A108
Alcalá, J. M., Manara, C. F., Natta, A., et al. 2017, A&A, 600, A20
Anderson, G. M. 1976, Geochim. Cosmochim. Acta, 40, 1533
Anderson, K. R., Adams, F. C., & Calvet, N. 2013, ApJ, 774, 9
Bouvier, J., Perraut, K., Le Bouquin, J. B., et al. 2020, A&A, 636, A108
Brasseur, C. E., Phillip, C., Fleming, S. W., Mullally, S. E., & White, R. L. 2019, Astrocut: Tools for creating cutouts of TESS images, Astrophysics Source Code Library, ascl:1905.007
Briceño, C., Calvet, N., Hernández, J., et al. 2005, AJ, 129, 907
Briceño, C., Calvet, N., Hernández, J., et al. 2019, AJ, 157, 85
Briceño, C., Vivas, A. K., Calvet, N., et al. 2001, Sci, 291, 93
Calvet, N., Briceño, C., Hernández, J., et al. 2005, AJ, 129, 935
Calvet, N., & Gullbring, E. 1998, ApJ, 509, 802
Cardelli, J. A., Clayton, G. C., & Mathis, J. S. 1989, ApJ, 345, 245
D'Alessio, P., Calvet, N., & Hartmann, L. 2001, ApJ, 553, 321

D'Alessio, P., Calvet, N., Hartmann, L., Franco-Hernández, R., & Servín, H. 2006, ApJ, 638, 314
D'Alessio, P., Calvet, N., Hartmann, L., Lizano, S., & Cantó, J. 1999, ApJ, 527, 893
D'Alessio, P., Calvet, N., Hartmann, L., Muzerolle, J., & Sitko, M. 2004, in IAU Symp. 221, Star Formation at High Angular Resolution, ed. M. G. Burton, R. Jayawardhana, & T. L. Bourke (Cambridge: Cambridge Univ. Press), 403
D'Alessio, P., Cantö, J., Calvet, N., & Lizano, S. 1998, ApJ, 500, 411
D'Alessio, P., Hartmann, L., Calvet, N., et al. 2005, ApJ, 621, 461
Dotter, A. 2016, ApJS, 222, 8
Dorschner, J., Begemann, B., Henning, T., et al. 1995, A&A, 300, 503
Draine, B. T., & Lee, H. M. 1984, ApJ, 285, 89
Dullemond, C. P., Dominik, C., & Natta, A. 2001, ApJ, 560, 957
Espaillat, C. C., Herczeg, G. J., Thanathibodee, T., et al. 2022, AJ, 163, 114
Espaillat, C. C., Robinson, C. E., Romanova, M. M., et al. 2021, Natur, 597, 41
Fischer, W., Edwards, S., Hillenbrand, L., & Kwan, J. 2011, ApJ, 730, 73
Fischer, W. J., Hillenbrand, L. A., Herczeg, G. J., et al. 2022, arXiv:2203.11257
Fitzpatrick, E. L., Massa, D., Gordon, K. D., Bohlin, R., & Clayton, G. C. 2019, ApJ, 886,108
France, K., Schindhelm, R., Herczeg, G. J., et al. 2012, ApJ, 756, 171
Frasca, A., Boffin, H. M. J., Manara, C. F., et al. 2021, A&A, 656, A138
Gaia Collaboration, Brown, A. G. A., Vallenari, A., et al. 2021, A&A, 649, A1
Gravity Collaboration 2020, Natur, 584, 547
Gullbring, E., Calvet, N., Muzerolle, J., & Hartmann, L. 2000, ApJ, 544, 927
Habing, H. J. 1968, Bull. Astron. Inst. Netherlands, 19, 421
Hartmann, L., Herczeg, G., & Calvet, N. 2016, ARA&A, 54, 135
Hartmann, L., Hewett, R., & Calvet, N. 1994, ApJ, 426, 669
Herczeg, G. J., & Hillenbrand, L. A. 2008, ApJ, 681, 594
Horne, J. H., & Baliunas, S. L. 1986, ApJ, 302, 757
Husser, T. O., Wende-von Berg, S., Dreizler, S., et al. 2013, A&A, 553, A6
Ingleby, L., Calvet, N., Herczeg, G., et al. 2013, ApJ, 767, 112
Ingleby, L., Calvet, N., Hernández, J., et al. 2014, ApJ, 790, 47
Ingleby, L., Espaillat, C., Calvet, N., et al. 2015, ApJ, 805, 149
Kausch, W., Noll, S., Smette, A., et al. 2015, A&A, 576, A78
Kenyon, S. J., & Hartmann, L. 1995, ApJS, 101, 117
Koenigl, A. 1991, ApJL, 370, L39
Kounkel, M., Covey, K., Moe, M., et al. 2019, AJ, 157, 196
Lindegren, L. 2020, A&A, 633, A1
Liseau, R., White, G. J., Larsson, B., et al. 1999, A&A, 344, 342
Manara, C. F., Ansdell, M., Rosotti, G. P., et al. 2022, arXiv:2203.09930
Manara, C. F., Frasca, A., Alcalá, J. M., et al. 2017, A&A, 605, A86
Manara, C. F., Frasca, A., Venuti, L., et al. 2021a, A&A, 650, A196
Manara, C. F., Frasca, A., Venuti, L., et al. 2021b, PENELLOPE–X-Shooter spectra of targets in the Orion OB1 and sigma-Orionis regions, Zenodo, doi:10.5281/zenodo.4477091
Manara, C. F., Testi, L., Rigliaco, E., et al. 2013, A&A, 551, A107
Mathis, J. S., Rumpl, W., & Nordsieck, K. H. 1977, ApJ, 217, 425
Maucó, K., Briceño, C., Calvet, N., et al. 2018, ApJ, 859, 1
Maucó, K., Hernández, J., Calvet, N., et al. 2016, ApJ, 829, 38
McClure, M. K., D'Alessio, P., Calvet, N., et al. 2013, ApJ, 775, 114
Muzerolle, J., Calvet, N., & Hartmann, L. 1998, ApJ, 492, 743
Muzerolle, J., Calvet, N., & Hartmann, L. 2001, ApJ, 550, 944
Muzerolle, J., Calvet, N., Hartmann, L., & D'Alessio, P. 2003, ApJL, 597, L149
Natta, A., Prusti, T., Neri, R., et al. 2001, A&A, 371, 186
Pecaut, M. J., & Mamajek, E. E. 2013, ApJS, 208, 9
Percy, J. R., Grynko, S., Seneviratne, R., & Herbst, W. 2010, PASP, 122, 753
Proffitt, C. R., Roman-Duval, J., Taylor, J. M., et al. 2021, RNAAS, 5, 36
Ricker, G. R., Winn, J. N., Vanderspek, R., et al. 2014, Proc. SPIE, 9143, 914320
Robinson, C. E., & Espaillat, C. C. 2019, ApJ, 874, 129
Roman-Duval, J., Proffitt, C. R., Taylor, J. M., et al. 2020, RNAAS, 4, 205
Scargle, J. D. 1982, ApJ, 263, 835
Schobert, B. N., & Peeters, A. G. 2021, A&A, 651, A27
Sergison, D. J., Naylor, T., Littlefair, S. P., Bell, C. P. M., & Williams, C. D. H. 2020, MNRAS, 491, 5035
Shu, F., Najita, J., Ostriker, E., et al. 1994, ApJ, 429, 781
Smette, A., Sana, H., Noll, S., et al. 2015, A&A, 576, A77
Tokovinin, A., Petr-Gotzens, M. G., & Briceño, C. 2020, AJ, 160, 268
Tuthill, P. G., Monnier, J. D., & Danchi, W. C. 2001, Natur, 409, 1012
Valenti, J. A., Basri, G., & Johns, C. M. 1993, AJ, 106, 2024
Venuti, L., Bouvier, J., Cody, A. M., et al. 2017, A&A, 599, A23
Venuti, L., Bouvier, J., Flaccomio, E., et al. 2014, A&A, 570, A82
Whittet, D. C. B., Shenoy, S. S., Clayton, G. C., & Gordon, K. D. 2004, ApJ, 602, 291